Total mechanical energy transport lines and attractors in separating turbulent boundary layers

Wen Wu, Rajat Mittal, and Charles Meneveau

Phys. Rev. Fluids **5**, 012601 — Published 23 January 2020

DOI: 10.1103/PhysRevFluids.5.012601

Total mechanical energy transport lines and attractors in separating turbulent boundary layers

Wen Wu,* Rajat Mittal, and Charles Meneveau
Department of Mechanical Engineering, Johns Hopkins University, Baltimore, MD 21218, USA
(Dated: January 10, 2020)

In order to provide new insights into the energetics of turbulent boundary layer flows with separation, we compute and characterize energy transport lines, which are defined as the lines tangent to the total mechanical energy transport vector field. Separation is induced in a $Re_\theta = 490$ turbulent boundary layer by imposing two types of transpiration velocity profiles at the top boundary of the computational domain: one with suction and blowing, and the other with suction only. For both separation bubbles, we find that energy transport lines can exhibit attractors, which are a manifestation of local dissipation in the flow. We identify several attracting sets along the bottom wall and attracting spiral nodes inside the separation bubbles and their corresponding basins of attraction. The size and positions of the energy basins of attraction help us understand where the available total mechanical energy is transported to due to the mean flow, and turbulent Reynolds and viscous stresses, before it is fully dissipated. The suction-and-blowing separation bubble leads to slightly smaller losses of total mechanical energy than those for a reference non-separated boundary layer, while the suction-only case shows larger losses than the non-separated boundary layer case.

The mean total mechanical energy per unit mass in a flow, $E = U_i U_i/2 + P/\rho$, where U_i is the mean velocity, P the mean pressure and ρ the fluid density, is one of the critical flow parameters used to assess the performance of thermo-fluid devices. For example, in diffusers, it represents the maximum pressure that could be recovered from the dynamic pressure; in high-speed aircraft and rockets, the loss of E is related to the aerodynamic heating of the solid body; for power-harvesting devices, E measures the amount of usable energy in the flow, etc. For applications whose performance is often degraded by flow separation, flow control to prevent separation is often aimed at reducing losses of E. To improve on our abilities to manipulate separated flows for such purposes, it is of interest to better visualize and characterize properties of the flow in a way that directly reflects the evolution of E.

For turbulent flows, if one wishes to visualize the mean velocity distribution, a traditional flow visualization tool is a streamline plot. Streamlines are the lines tangent to the mean velocity vector field (for simplicity in this paper we focus on turbulent flows with a steady mean). Mean flow streamlines represent how the fluid volume (or mass) is transported from one location to another. For incompressible flows, the vector field is divergence free, allowing analogies with trajectories in the phase space of Hamiltonian dynamical systems. As a result, streamlines do not exhibit attractors. For turbulent flows with losses, the connection between streamlines and total mechanical energy transport is less direct. As developed in Ref. [1], the notion of a transporting vector field can be generalized to quantities other than fluid volume or mass, and transport lines for linear momentum, energy and other quantities can be defined and visualized. Similarly so-called "heatlines" have been used in convection heat transfer to visualize the transport of heat [2]; scalar tubes were used to characterize the scalar transport in a turbulent jet [3]; kinetic energy lines were employed to understand the origin of energy arriving at wind turbines in studies of wind-farm efficiency ([1, 4]); vorticity tubes have been employed to explain vortex evolution [5]; and momentum, kinetic energy and exergy tubes were applied to investigate transport phenomena occurring in a supersonic ejector [6, 7].

In this study, we focus on the transport of E in flows including separation. The objective is to visualize the trajectory of energy transport and to provide insights into the energy loss process during flow separation. Compared to a control volume analysis, the energy transport lines provide further information about the direction of energy transport and attractors of energy. Using energy lines, we also estimate the energy gain/loss in the flow and discuss how energy carried by different portions of the incoming boundary layer, is consumed as it is transported through the region of flow separation.

The transport equation for the total mean-flow mechanical energy reads [1]

$$\frac{\partial F_{E,j}}{\partial x_j} = -\left(-\overline{u_i' u_j'}\frac{\partial U_i}{\partial x_j} + 2\nu S_{ij} S_{ij}\right) \tag{1}$$

where $\mathbf{F}_E$ is the total mechanical energy transport vector defined as

$$F_{E,j} = E\, U_j + \overline{u_i' u_j'}\, U_i - 2\nu S_{ij}\, U_i, \tag{2}$$

* wenwu.cfd@gmail.com

and ν is the kinematic viscosity and S_{ij} is the mean-flow strain-rate tensor. As can be seen in Eq. 2, in the absence of turbulence and viscous stresses, the transport vector field of E is parallel to the mean velocity U_i and energy transport lines coincide with streamlines. Eq. 1 is in the form of $\nabla \cdot \mathbf{F}_E = -\varepsilon$, where the total dissipation ε consists of the two terms on the right-hand-side (RHS) of Eq. (1). These are the sinks/sources (depending on the term's sign) due to the production of turbulent kinetic energy (TKE) $-\overline{u_i' u_j'} \frac{\partial U_i}{\partial x_j}$, and the mean-flow viscous dissipation, respectively. The TKE production is most often positive, thus acting as a sink of mean energy. When there is backscatter of TKE, however, this term is a source of E, while the viscous dissipation is always a sink of the energy.

An energy line is defined in a similar way as a streamline, but with respect to the energy transport vector field ($\mathbf{F}_E$) instead of the velocity field, i.e. the lines tangent to $\mathbf{F}_E$. Energy lines that start at points that form a closed loop (in 3D, or the end-points of a segment in 2D), form an energy transport tube that is "impermeable" for energy transport [1]. It should be noted that unlike streamtubes in incompressible flow, the cross-sectional area of an energy transport tube does not give information regarding the local magnitude of the transport velocity, because energy is not conserved along an energy tube.

In this paper we present visualizations and analysis of the vector field $\mathbf{F}_E$ for boundary layer flows that involve flow separation, with special attention to the process of energy loss and the corresponding attractors. The data used for the study are from DNS of two types of separation bubbles induced on a turbulent boundary layer (TBL) developing on a flat plate. The DNS has previously been described in [8], and while a brief overview of the configuration and simulation methodology is provided here, the reader is referred to [8] for further details. Comparisons with energy lines in a non-separating canonical TBL are also presented.

The separating TBLs under investigation are subjected to a streamwise pressure gradient (PG) created by a transpiration velocity (V_{top}) imposed at the upper boundary (see Fig. 1). Two cases are considered: (a) with suction-blowing denoted as 'TSB-SB', and (b) suction-only, denoted 'TSB-SO'. The Reynolds number of the reference inlet TBL is $Re_\theta = U_o \theta_o / \nu = 490$ (where U_o and θ_o are the freestream velocity and momentum thickness at the reference plane). Similar flow configurations have been used in the literature to study flow separation [9–13], but not much attention has been devoted to studying the process of mechanical energy transport in such flows. The transpiration velocity profiles are designed such that the adverse PGs before the crest of the separation bubble agree well between the two cases.

A domain size of $100\theta_o \times 117\theta_o$ in the wall-normal and spanwise directions, is used for both cases. In the streamwise direction, the domain is $x \in [-200, 735]\theta_o$ for the TSB-SB case and $x \in [-200, 970]\theta_o$ for TSB-SO, among which $x \in [-200, -78]\theta_o$ is used for the recycling and rescaling method [14] to generate a physical inflow turbulence. The grid spacing at the reference plane is $\Delta x^+ = 9.6$ (9.0), $\Delta y_1^+ = 0.58$ (0.58), and $\Delta z^+ = 7.2$ (7.2) for TSB-SB (TSB-SO) in wall units. Away from the wall, the grid size ($\sqrt{\Delta x^2 + \Delta y^2 + \Delta z^2}$) is less than twice the local Kolmogorov length scale everywhere.

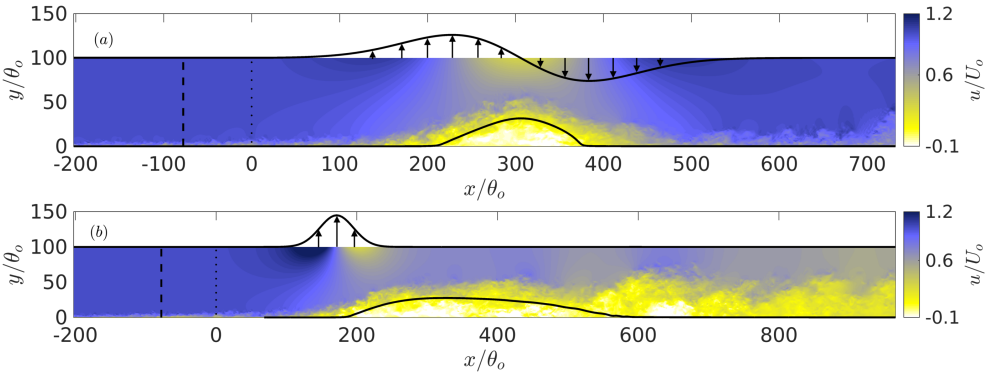

FIG. 1. Contour plots of streamwise velocity in snapshots of the simulations, also showing aspects of the DNS configuration. *(a)*, TSB-SB case; *(b)*, TSB-SO case. Dashed vertical line: recycling plane; dotted vertical line: reference plane; Thick solid line near the top boundary corresponds to a profile of $50V_{\text{top}}/U_o + 100$; the thin solid line shows the separating streamline of the mean flow.

With the prescribed V_{top}, a zero spanwise vorticity condition is used for U and zero wall-normal gradient condition for W (U, V, W denote the mean velocity component in the streamwise, wall-normal and spanwise directions, respectively; mean turbulent quantities will be denoted as $\overline{(.)}$). For the inflow, a standard recycling and rescaling method [14] with constant spanwise shift [15] is used (see Fig. 1), which provides a zero-pressure-gradient (ZPG) TBL inflow. The PG however starts further downstream from the reference plane (*i.e.*, x=0 and the Clauser pressure-gradient parameter is below 0.5 until $x/\theta_o = 60$). Periodic boundary conditions are used in the spanwise direction

and a convective boundary is imposed at the outlet [16]. We employ a very long and wide domain to ensure that the large-scale turbulent structures in the separating and reattachment region are not affected by the domain size [8]. The calculations are carried out using a well-established finite-difference flow solver for incompressible Navier-Stokes equations on a Cartesian, cell-centered grid [17, 18].

Some comparisons with non-separating ZPG TBL will also be performed. Those data are obtained from the fully-developed region in the DNS of a transitioning boundary layer [19] available in a public database. Velocity data are extracted starting at a reference location at $Re_\theta = 490$ so as to be comparable to the separating boundary layer cases.

The analysis presented in Ref. [8] focused on the spatio-temporal fluctuations of the flow. In particular, the TSB-SO case was shown to generate a low-frequency motion that appears as a slow merging of the spanwise roller vortices in the separated shear layer and the formation of large-scale discrete vorticity packets. Here we focus instead on the transport and evolution of the mechanical energy contained in the mean flow. For purposes of the present analysis, statistics are collected over a long time duration corresponding to about 14,000 θ_o/U_o, and starting after the flow has transitioned from the initial conditions. In addition to time averaging, data are also averaged over the spanwise direction for these flows with nominally 2D mean distributions. Contour plots of total mean mechanical energy $E(x, y)$ for the two TSB cases are shown in Fig. 2. It can be seen that there is significant spatial variation of $E(x, y)$ across the shear layer, both when it is attached to the wall and when it separates. Inside the separation bubble, both the mean velocity (with small magnitude) and the pressure show little variation, leading to a quite uniform E.

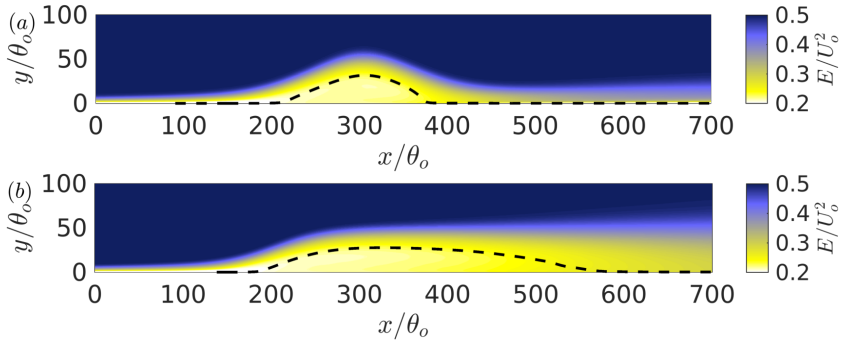

FIG. 2. Contour plots of the mean total mechanical energy density $E(x, y)$. *(a)*, TSB-SB; *(b)*, TSB-SO. The dashed line shows the separating streamline.

Mean velocity, pressure, and Reynolds stress distributions are evaluated in all cases from the DNS and streamlines and lines tangent to $\mathbf{F}_E$ (according to Eq. (2)) are evaluated. Results are shown in Fig. 3 for the two cases with flow separation. The figure also includes a color contour representation of the right-hand-side (RHS) of Eq. (1), *i.e.* the local rate of dissipation and TKE production, that is equal to the divergence of $\mathbf{F}_E$. To facilitate comparisons of the different types of lines, the starting points for streamlines and energy lines coincide at the same y locations, at $x = 0$.

It can be seen in Figs. 3 that the energy lines deviate from the streamlines, especially in regions where the RHS

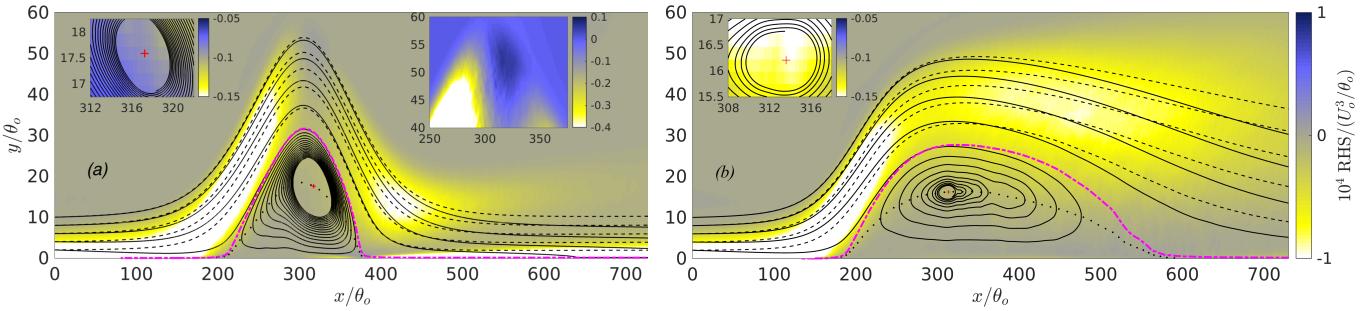

FIG. 3. Selected mean-flow streamlines (dashed lines) and energy transport lines (solid lines). *(a)*, TSB-SB; *(b)*, TSB-SO. The streamlines and energy lines are plotted starting from $x = 0$, y/θ_o= 2, 4, ..., 10. The source/sink of energy (*i.e.*, the right-hand-side (RHS) of Eq. (1)) is shown with filled contours. Energy lines near the spiral node attractor inside the separation bubble are not plotted for clarity; a closer view is shown in the upper-left inset. The upper-right inset in *(a)* shows the source of energy (*i.e.*, positive RHS of Eq. (1)) near the crest of the TSB-SB bubble. The dotted line denotes the locus of $U = 0$. The dash-dotted line is the separating streamline. The center of the attractor inside the bubble is marked by + ($[x, y]/\theta_o = [317.3, 17.6]$ for TSB-SB, $[313.6, 16.2]$ for TSB-SO). The y-axis is stretched by a factor of 5 for clarity.

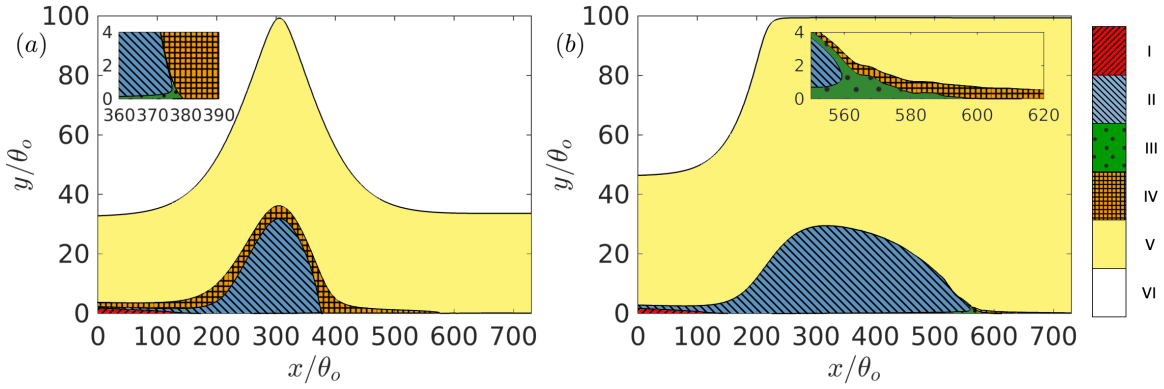

FIG. 4. Basins of the energy attractors in TSB-SB *(a)* and TSB-SO *(b)*. The classification for the various regions I-VI is described in the text. The various solid lines mark energy transport lines that act as boundaries between the basins of attraction. The y-axis is stretched by a factor of 5 for clarity.

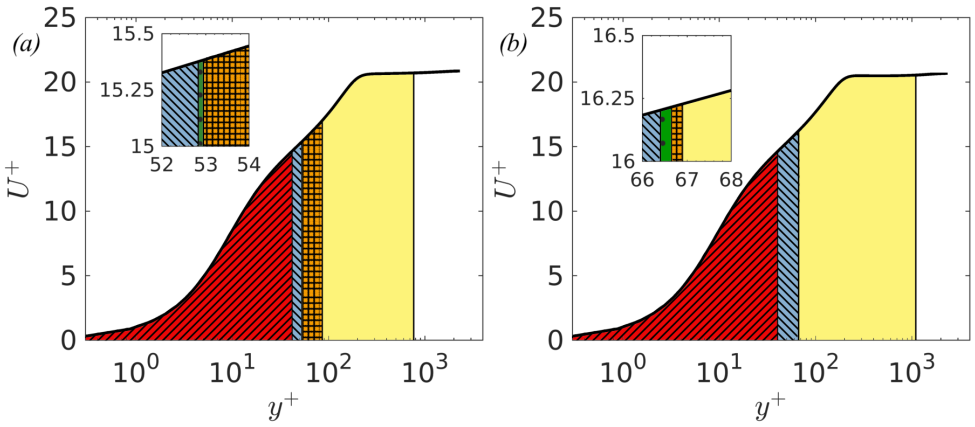

FIG. 5. Basins of the energy attractors at $x = 0$ with reference to the mean streamwise velocity in wall units. *(a)*, TSB-SB; *(b)*, TSB-SO. The classification for the five regions refer to the text.

of Eq. 1 is significant. In both cases, the high RHS regions are near the wall (where viscous dissipation is dominant) and in the separated shear layers (where TKE production is dominant). Near the crest of the separation bubble in the TSB-SB case, there is a region with mild positive RHS, indicating a "backscatter" from the turbulent kinetic energy into mean flow. The magnitude of such backscatter is much lower than the negative sink effect observed in most of the domain. The negative TKE production in such region has also been reported in the literature by Spalart & Coleman [20], Abe [11], Coleman et al. [13], Wu et al. [12], among others. Note that from our data we can see that the entire RHS of Eq. (1) acts as a net source of the energy, which includes the source due to the backscatter of TKE and a viscous sink due to the mean shear. Clearly, the source dominates the sink and thus leads to a net production of mean total mechanical energy.

Also apparent is the existence of a spiral node attracting fixed point for the energy transport lines that is located inside the separation bubbles. Energy transport lines thus cross into the separation bubble and terminate in this attracting point. The rate at which the inward spiralling takes place is different between the two cases: for the TSB-SB case, the rate is very slow, leading to almost neutrally stable periodic orbits due to the very low rate of total dissipation there. However, dissipation is not exactly zero and therefore some attraction is still present. For the TBL-SO case, the dissipation is larger, leading to faster rate of inward spiralling of the energy transport lines. For example, the average total sink of energy in a $5\theta_o$ by $1\theta_o$ $(x-y)$ box centered at the spiral node is -0.916×10^{-5} $U_o^3\theta_o^{-1}$ for TSB-SB and -1.45×10^{-5} $U_o^3\theta_o^{-1}$ for TSB-SO. In the two cases, the location of the spiral node attractor does not differ by much because the adverse PG and the front part of the separation bubbles are quite similar. Ref. [1] also observed a spiral node attractor (as well as saddles) of mechanical energy lines on Poincaré sections in the wind-turbine-array boundary layers in some parts of the flow, for certain turbine spacings.

The other attracting sets in this flow occur along the bottom wall. As shown for laminar wall-bounded flows in Ref. [1], the wall is an attractor of energy transport lines in viscous flow. Here we distinguish three distinct wall-regions:

the wall upstream of the separation bubble, the wall inside the separation bubble, and the wall downstream of the separation bubble. Associated with each of these attracting sets, we may identify a "basin of attraction". The flow field can thus be decomposed into four basins of attraction:

- Basin I: Region from which the energy ends up on the wall upstream of the mean separation bubble;
- Basin II: This is the basin of attraction of the spiral node attractor inside the separation bubble;
- Basin III: Region for which the energy ends up at the wall but inside the separation bubble;
- Basin IV: The energy ends up on the wall downstream of the mean reattachment point;

In addition, we can also identify Basin V as the region for which energy lines leave from the outflow location at $x/\theta_o = 730$ (because the TSB-SB case has a relatively shorter streamwise domain than TSB-SO, this location is selected as the downstream section to measure and compare the energy loss between these two cases) but without leaving (or re-entering) the domain from the top boundary, and Basin VI for which the energy goes out/in from the top boundary of the present computational domain. Energy that travels in Region VI is in the inviscid flow therefore is conserved and its trajectory collapses with the streamline (the imposed freestream pressure is already in E). Since we focus on the deviation of energy transport from the mass transport and the energy loss in this paper, Region VI is not of concern for the present study.

The various basins of attraction/regions are shown in Figure 4. The region for Basin I is the same in the two cases since the portion of the flow in front and near the separation bubble is very similar. The basin for the spiral node (Basin II) occupies a larger area in the TSB-SO case because of the bigger reversed-flow region; Basin III whose attractor is on the wall inside the separation bubble is negligible in both cases; and Basin IV is significantly reduced in the TSB-SO case compared to the TSB-SB case, because the flow is reattached by turbulent diffusion in the separated shear layer and the other sink term due to near-wall mean shear is weak.

Another representation of the basins of attraction in both cases can be made referring only to the incoming TBL, as shown in Figure 5. The energy in the viscous sublayer and buffer layer are entirely dissipated before flow separation (i.e., Basin I). The log-law region (though very limited due to the low Reynolds number), contributes to Basins II-IV. Much of the contributions to Basins II-IV originates in the the log-law region of the incoming TBL (though limited due to the moderate Reynolds number). Note that Abe [11] observed that the effect of the active motions in an incoming TBL dominate the dynamics downstream in the separated region. Our results help connect the incoming log-layer to the dynamics in the separated regions from the viewpoint of mechanical energy. A significant portion of the energy within the TBL (i.e., in the outer layer, Basin V) is only partially consumed even when the flow reaches $x/\theta_o = 730$. However, it is understood that eventually, if the TBL extends to larger x/θ_o values, the entire kinetic energy is dissipated as it is transported along the energy lines ending at the wall. Note that Basins III and IV could have been combined into a single region defined as the region where all transport lines end up on the wall downstream of the separation point. However, making reference to the mean flow streamlines allows us to distinguish regions inside and downstream of the mean flow separation bubble.

Figure 6(a) shows energy transport lines for Basins I+II+III+IV in both cases with separation, as well as the ZPG TBL case for which there is only a single wall attractor. In order to measure the energy loss between energy lines, we calculate the total E flux (i.e., $\int (F_E)_1 dy$) per unit width at $x = 0$ and any x/θ_o, and obtain the energy loss from their difference according to $\int (F_E)_1 dy(x) - \int (F_E)_1 dy(0)$. Equivalently using the divergence theorem, one may also evaluate the area integral of the total dissipation between the lines (although that calculation is more cumbersome). Results are shown in Fig. 6(b) for the various flow cases. Comparing the energy lines for the union of all four basins for which the attractors are in the computational domain (i.e. Basins I+II+III+IV) (blue lines), it appears that the ZPG TBL is the most dissipative when comparing the energy losses associated with the flow in regions terminating in these attractors. It has the largest basin of attraction, and a larger fraction of the energy flux entering at $x = 0$ is dissipated at the wall for this case than for the cases with separation. This is because the mean shear in these regions becomes weaker due to the absence of the wall after flow detaches. The maximum shear occurs in the middle of the separated shear layer, which contributes to the energy loss in Basin V (but this energy is not lost completely within the calculation domain while the energy in Basin I to IV is entirely dissipated). For engineering applications, this would e.g. indicate less aerodynamic heating at the wall within and around the separation region. For the ZPG TBL, the energy line starting at $y/\theta_o = 20$ can be seen to have a small positive slope (total energy slowly moving away from the wall). That is because it is far outside the TBL and thus coincides exactly with the standard streamline there, which has a small positive slope due to the displacement velocity of the TBL.

The energy loss rate (energy loss per x-distance) in the TSB-SB case after flow reattachment seems to be similar to the one in the ZPG TBL: in Fig. 6 (b) the solid line represents the energy loss in the ZPG TBL case and the lines with triangles describe the energy loss of the reattached flow. The slope of the former agrees quite well with the later one for the TSB-SB case (dashed line with triangle). The TSB-SO case (dash-dotted line with triangle) shows

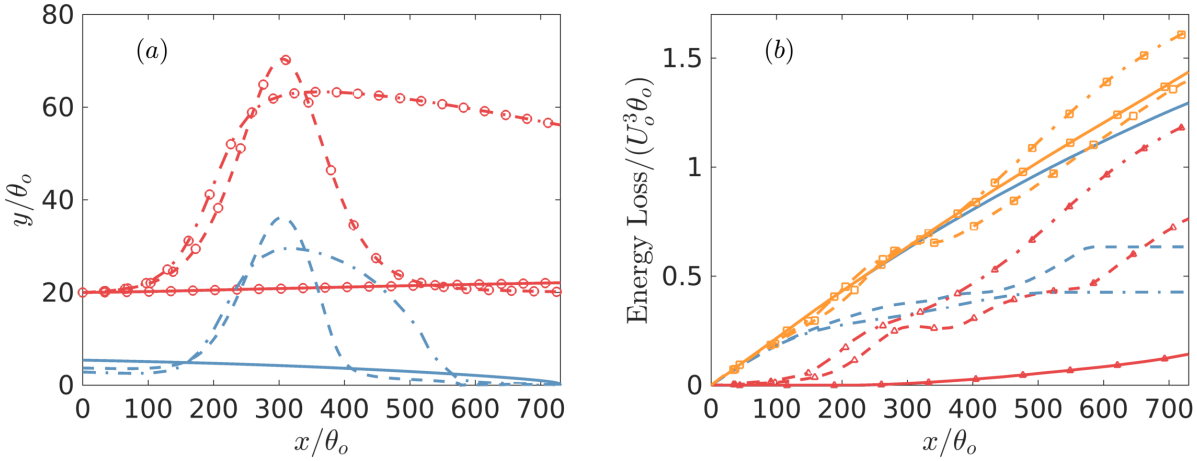

FIG. 6. (a) Comparison of energy transport lines separating Basins I+II+III+IV from Region V (lines), and between Region V and a location outside all dissipative regions (inflow below $y/\theta_o = 20$)(lines with circle), for the three flows considered: TSB-SB (dashed lines), TSB-SO (long dashes and dots), and ZPG TBL [19] (solid lines). (b) shows the downstream evolution of the total energy loss between the lines shown in (a): lines without symbol measure between the lines in (a) and the wall, and lines with triangles measure between the lines and lines with symbols in (a); lines with open square show the total energy loss in the flow domain.

a slightly faster decay. This is reasonable because the reattached flow in the TSB-SB case losses energy mainly due to the viscous sink by the near-wall shear. The contribution of turbulence, which may be affected by the recovery of the flow to the canonical boundary layer [21, 22] , is smaller. In the TSB-SO case, however, the energy in this region is consumed by the turbulence in the separated shear layer.

Summarizing, we observe that the total energy lost is highest for the TSB-SO case, as by the time the end of the domain is reached at $x/\theta_o = 730$, the integrated loss is $1.624\,U_o^3\theta_o$ (having units of energy flux times length, or energy dissipation rate times area). The next one is the ZPG case with integrated loss of $1.471\,U_o^3\theta_o$. Finally, and perhaps surprisingly, the TSB-SB case has the lowest total energy loss, at $1.396\,U_o^3\theta_o$. As shown by Fig. 6, the difference of the integrated loss between the TSB-SB and TSB-SO is mainly due to the energy loss in Basin V, i.e., in the separated shear layer, where the energy loss in TSB-SO is significantly higher than it in the TSB-SB and ZPG TBL. It is likely due to the fact that the TSB-SO case has large-scale turbulent structures and higher TKE downstream of the crest of the separation bubble [8]. The intensive turbulent diffusion appears as the separated shear layer undergoes three-dimensionalization during its slow reattachment (without the forced reattachment), and acts as a strong sink for mechanical energy. For the TSB-SB, the backscatter of TKE near the crest of the bubble diminishes the sink and the energy loss in the outer part of the forced reattached shear layer is weak, thus leading to much smaller energy losses (refer to Fig. 3 and [8]). Far away from the bottom wall (i.e., outside of the TBL, the flow is inviscid and the energy is conserved.

It is interesting to note, therefore, that flow separation by itself may not always cause larger energy loss as compared to the fully attached TBL case. In this case, the TSB-SB case shows slightly lower energy losses compared to the attached case, although it appears to be approaching the same total losses.

In conclusion, we have explored the transport and change of the total mechanical energy during pressure-induced flow separation over a flat plate and compared two cases with separation with a canonical attached TBL case. The main results of our analysis are visualizations of the fate of total mechanical energy in the flow through the energy transport lines. We observe attractors, which are never present in streamline patterns of incompressible flow and for which the kinematics are Hamiltonian. Results show a spiral node attractor inside the separation bubbles and three segments of the walls are identified as attracting sets of the energy transport lines. The basins of attraction of these attractors in the entire flow and for the incoming TBL are identified and serve to classify regions in the flow. The total energy loss as function of downstream distance within several of these regions is quantified and explained. While this analysis does not provide a simple conclusion about which configuration can preserve more total mechanical energy, it shows that it is lost by different mechanisms in different regions of the flow.

The authors were supported by AFOSR Grant FA9550-17-0084. The authors would like to thank Drs. L. Cattafesta (Florida State University), C. Rowley (Princeton University) and D. Gayme (Johns Hopkins University) for fruitful

discussions.

[1] J. Meyers and C. Meneveau, Flow visualization using momentum and energy transport tubes and applications to turbulent flow in wind farms, J. Fluid Mech. **715**, 335 (2013).

[2] S. Kimura and A. Bejan, The heatline visualization of convective heat transfer, Journal of Heat Transfer **105**, 916 (1983).

[3] A. Önder and J. Meyers, Modification of vortex dynamics and transport properties of transitional axisymmetric jets using zero-net-mass-flux actuation, Phys. Fluids **26**, 075103 (2014).

[4] D. Allaerts and J. Meyers, Gravity waves and wind-farm efficiency in neutral and stable conditions, Boundary-Layer Meteorol **166**, 269 (2018).

[5] J. Schröttle, A. Dörnbrack, and U. Schumann, Gravity waves and wind-farm efficiency in neutral and stable conditions, Fluid Dynamics Research **47**, 035508 (2015).

[6] O. Lamberts, P. Chatelain, and Y. Bartosiewicz, New methods for analyzing transport phenomena in supersonic ejectors, Intl. J. Heat Fluid Flow **64**, 23 (2017).

[7] Y. Fang, S. Poncet, and Y. Bartosiewicz, Analysis of transport phenomena in a two-phase co_2 supersonic ejector, in *Proceedings of the 27th CANCAM* (2019).

[8] W. Wu, C. Meneveau, and R. Mittal, Spatio-temporal dynamics of turbulent separation bubbles, J. Fluid Mech. **883**, A45 (2020).

[9] Y. Na and P. Moin, Direct numerical simulation of a separated turbulent boundary layer, J. Fluid Mech. **374**, 379 (1998).

[10] P. R. Spalart and M. K. Strelets, Mechanisms of transition and heat transfer in a separation bubble, J. Fluid Mech. **403**, 329 (2000).

[11] H. Abe, Reynolds-number dependence of wall-pressure fluctuations in a pressure-induced turbulent separation bubble, J. Fluid Mech. **833**, 563 (2017).

[12] W. Wu and U. Piomelli, Effects of surface roughness on a separating turbulent boundary layer, J. Fluid Mech. **841**, 552 (2018).

[13] G. N. Coleman, C. L. Rumsey, and P. R. Spalart, Numerical study of turbulent separation bubbles with varying pressure gradient and reynolds number, J. Fluid Mech. **847**, 28 (2018).

[14] T. Lund, X. Wu, and K. Squires, Generation of turbulent inflow data for spatially- developing boundary layer simulations, J.Comput. Phys. **140**, 233 (1998).

[15] P. R. Spalart, M. Strelets, and A. Travin, Direct numerical simulation of large-eddy-break-up devices in a boundary layer, Intl. J. Heat Fluid Flow **27**, 902 (2006).

[16] I. Orlanski, A simple boundary condition for unbounded hyperbolic flows, J. Comput. Phys. **21**, 251 (1976).

[17] R. Mittal, H. Dong, M. Bozkurttas, F. Najjar, A. Vargas, and A. von Loebbecke, A versatile sharp interface immersed boundary method for incompressible flows with complex boundaries, J. Comp. Phys. **227**, 4825 (2008).

[18] W. Wu, J.-H. Seo, C. Meneveau, and R. Mittal, Response of a laminar separation bubble to forcing with zero-net mass flux jets, in *Proc. 2018 Flow Control Conference, AIAA AVIATION Forum, (AIAA 2018-4018)* (2018).

[19] T. A. Zaki, From streaks to spots and on to turbulence: exploring the dynamics of boundary layer transition, Flow, Turbulence and Combustion **91**, 451 (2013).

[20] P. R. Spalart and G. N. Coleman, Numerical study of a separation bubble with heat transfer, Eur. J. Mech. (B/Fluids) **16**, 169 (1997).

[21] C. Chandrsuda and P. Bradshaw, Turbulence structure of a reattaching mixing layer, J. Fluid Mech. **110**, 171 (1981).

[22] H. Abe, Direct numerical simulation of a turbulent boundary layer with separation and reattachment over a range of reynolds numbers, Fluid Dyn. Res. **51**, 011409 (2019).